Supporting Information

Bimetallic ruthenium-nickel alloy nanostructure supported on nickel foam for efficient alkaline hydrogen evolution at large current density

Xiaoqing Mao[a], Zhihang Liu[b], Changqing Lin[c], Jiawang Li[c], Pei Kang Shen[a],*

[a] School of Chemistry and Chemical Engineering, Collaborative Innovation Center of Sustainable Energy Materials, Guangxi University, Nanning 530004, P. R. China.

[b] School of Resources, Environment and Materials, Guangxi University, Nanning 530004, P. R. China.

[c] School of Physical Science and Technology, Guangxi University

*Corresponding author E-mail: pkshen@gxu.edu.cn.

1. Experimental sections

1.1. Chemicals and Reagents

Ruthenium chloride hydrate ($RuCl_3 \cdot 3H_2O$, Sinopharm Chemical), Nickel(II) Chloride Hexahydrate Puratrem ($NiCl_2 \cdot 6H_2O$, Sinopharm Chemical), ethanol (C_2H_6O, Sinopharm Chemical). Hexadecyl trimethyl ammonium Bromide (CTAB) was purchased from Macklin. All the chemicals and reagents are of analytical grade and used without further purification. Double-distilled water was used throughout the experiment.

1.2. Synthesis of Ru-Ni alloy.

The Ru-Ni alloy nanosheets were prepared by hydrothermal method. A piece of nickel foam (20.0 mm×20.0 mm) was washed with 3 M HCl, ethanol and deionized water for 15 minutes respectively. Then 120 mg $NiCl_2·6H_2O$, 20 mg $RuCl_3·3H_2O$ and 135 mg CTAB were dissolved in 15 ml ethanol and stirred for 20 minutes to form a uniform solution. The solution and treated nickel foam were then transferred to 25 ml Teflon lined stainless steel autoclave. The autoclave was maintained at 180 °C for 12 hours. After the reaction was finished, the nickel foam loaded with the precursor was washed with deionized water and then dried dried in vacuum at 60 °C for 5 h. The sample was named RuNi-20/NF. For comparison, RuNi-10/NF and RuNi-30/NF were synthesized by the same method with adding 10 mg $RuCl_3·3H_2O$ and 30 mg $RuCl_3·3H_2O$. Ru/NF was synthesized by the same method without adding $NiCl_2·6H_2O$.

1.3. Synthesis of Ni/NF nanosheets

The Ni/NF was synthesized by the same method but without adding $RuCl_3·3H_2O$ and then annealing under H_2 at 400 °C for 2 hours.

1.4. Synthesis of 20wt%Pt/C/NF

5.0 mg 20 wt% Pt/C was dispersed in 1.0 mL solution contain 20.0 μL 5.0 wt% Nafion solution and 0.98 mL ethanol. Then it was treated by ultrasonic for about 15 min. Finally, Pt/C/NF was formed by dropping 10.0 μL above solution on the surface of NF.

1.5. Materials characterization

Powder X-ray diffraction (XRD) patterns were employed on a SMARTLAB3KW X-ray diffractometer with Cu Kα radiation (40 kV 30 mA) of λ = 0.154 nm at room temperature (Rigaku, Japan). Scanning electron microscope (SEM) analysis was performed on a SU8220 (FE-SEM, Hitachi, Japan) scanning electron microscope at an accelerating voltage of 10 kV. Transmission electron microscope (TEM) measurements were obtained on a Titan G^2 80-300 (FEI company, American) electron mocroscope. X-ray photoelectron spectroscopy (XPS) experiments were carried out on an ESCALAB 250XI+ (Thermo Fisher Scientific company, USA) X-ray photoelectron spectrometer using Al as the exciting source.

1.6. Electrochemical measurements

All the catalysts were evaluated in 1 M KOH aqueous solution using a conventional three-electrode configuration. The nickel foams loaded with catalyst were used as the working electrodes. The Hg/HgO electrode and graphite rod electrode were used as reference electrode and counter electrode, respectively. Electrochemical impedance spectroscopy (EIS) measurements were recorded at the open-circuit potential in the frequency range of 10^5 Hz to 10^{-1} Hz.

2. Computational method

We have employed the Vienna Ab Initio Package (VASP) to perform all the density functional theory (DFT) calculations within the generalized gradient approximation (GGA) using the PBE formulation. We have chosen the projected augmented wave (PAW) potentials to describe the ionic cores and take valence electrons into account using a plane wave basis set with a kinetic energy cutoff of 400 eV. Partial occupancies of the Kohn−Sham orbitals were allowed using the Gaussian smearing method and a width of 0.05 eV. The electronic energy was considered self-consistent when the energy change was smaller than 10^{-5} eV. A geometry optimization was considered convergent when the force change was smaller than 0.02 eV/Å. Grimme's DFT-D3 methodology was used to describe the dispersion   interactions.

The equilibrium lattice constants of HCP-Ni unit cell were optimized, when using a 15×15×11 Monkhorst-Pack k-point grid for Brillouin zone sampling, to be a=2.480 Å, c=4.010 Å. We then use it to construct a Ni(001) surface model (model 1) with $p(3×3)$ periodicity in the x and y directions and 4 atomic layers in the z direction separated by a vacuum layer in the depth of 15 Å in order to separate the surface slab from its periodic duplicates. In another model (model 3), 1/3 of Ni atoms in model 1 were replaced by Ru atoms. The equilibrium lattice constants of HCP-Ru unit cell were optimized, when using a 15×15×11 Monkhorst-Pack k-point grid for Brillouin zone sampling, to be a=2.698 Å, c=4.262 Å. We

then use it to construct a Ru(001) surface model (model 2) with $p(3 \times 3)$ periodicity in the x and y directions and 4 atomic layers in the z direction separated by a vacuum layer in the depth of 15 Å in order to separate the surface slab from its periodic duplicates. During structural optimizations, a $3 \times 3 \times 1$ k-point grid in the Brillouin zone was used for k-point sampling, and the bottom two atomic layers were fixed while the top two were allowed to relax.

The adsorption energy (E_{ads}) of adsorbate A was defined as

$E_{ads} = E_{A/surf} - E_{surf} - E_{A(g)}$, where $E_{A/surf}$, E_{surf} and $E_{A(g)}$ are the energy of adsorbate A adsorbed on the surface, the energy of clean surface, and the energy of isolated A molecule in a cubic periodic box with a side length of 20 Å and a $1 \times 1 \times 1$ Monkhorst-Pack k-point grid for Brillouin zone sampling, respectively.

The free energy of a gas phase molecule or an adsorbate on the surface was calculated by the equation $G = E + ZPE - TS$, where E is the total energy, ZPE is the zero-point energy, T is the temperature in kelvin (298.15 K is set here), and S is the entropy. The reported standard hydrogen electrode (SHE) model was adopted in the calculations of Gibbs free energy changes (ΔG) of all reaction steps, which was used to evaluate the reaction barrier. The chemical potential of a proton-electron

pair, $\mu(H^+) + \mu(e^-)$, is equal to the half of the chemical potential of one gaseous hydrogen molecule, $1/2\mu(H_2)$, at U = 0 V vs SHE at pH = 0.
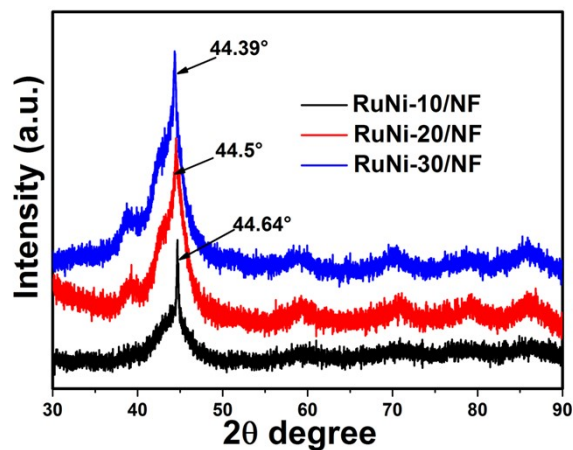

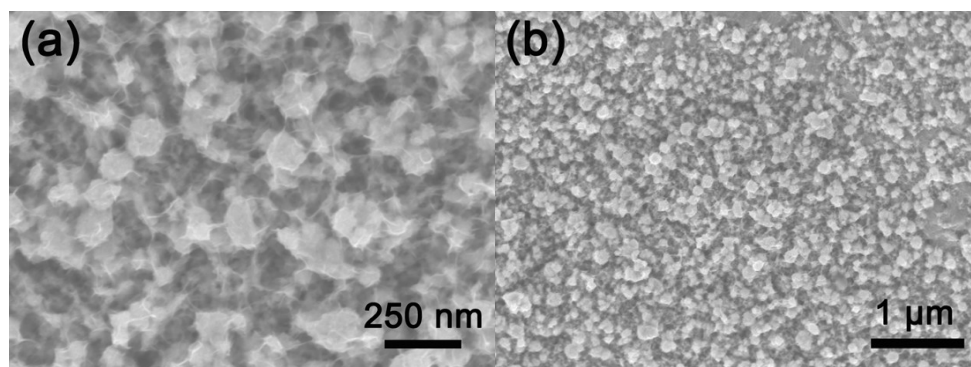**Figure S1.** XRD patterns of RuNi-10/NF, RuNi-20/NF and RuNi-30/NF.

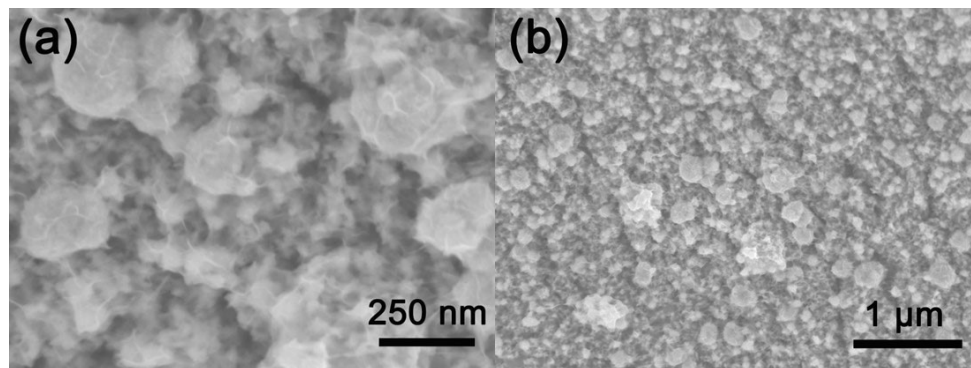
Figure S2. (a,b) SEM images of RuNi-10/NF.
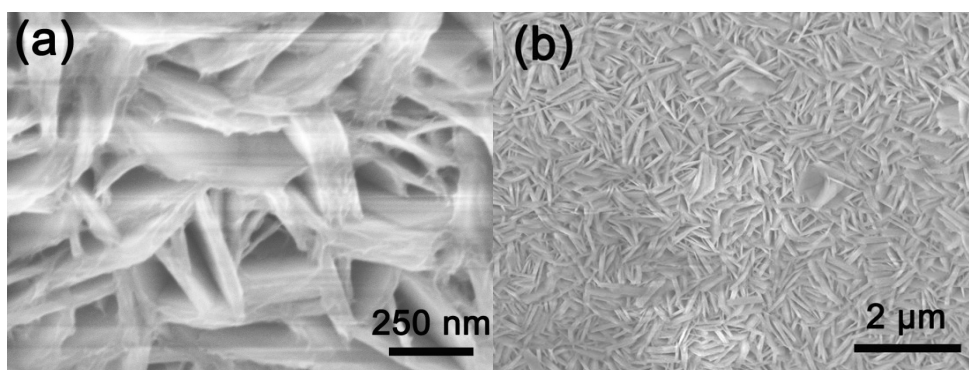

Figure S3. (a,b) SEM images of RuNi-30/NF.

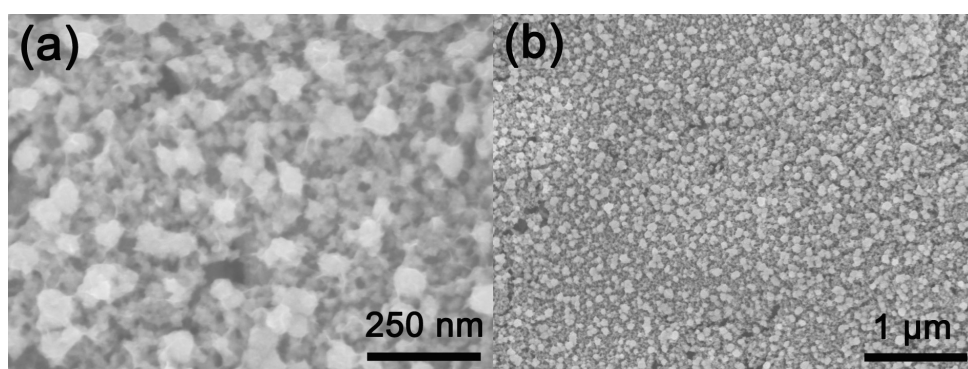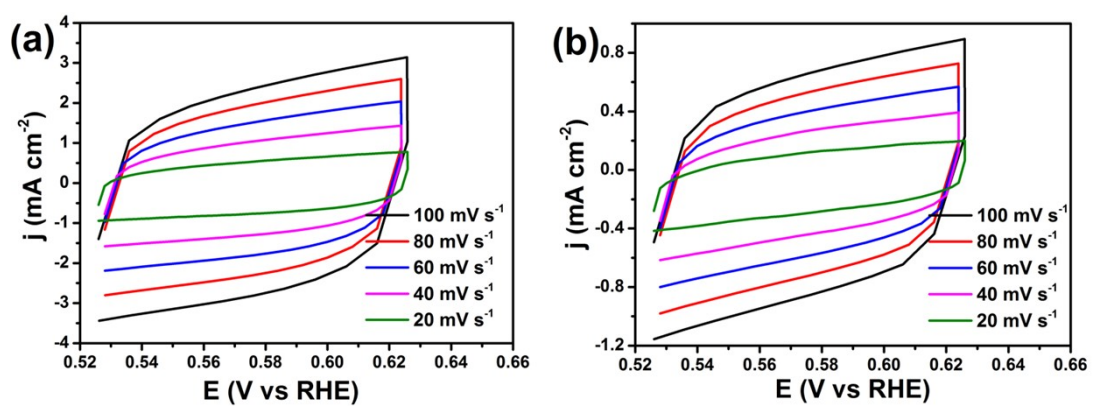**Figure S4.** (a,b) SEM images of Ni/NF.
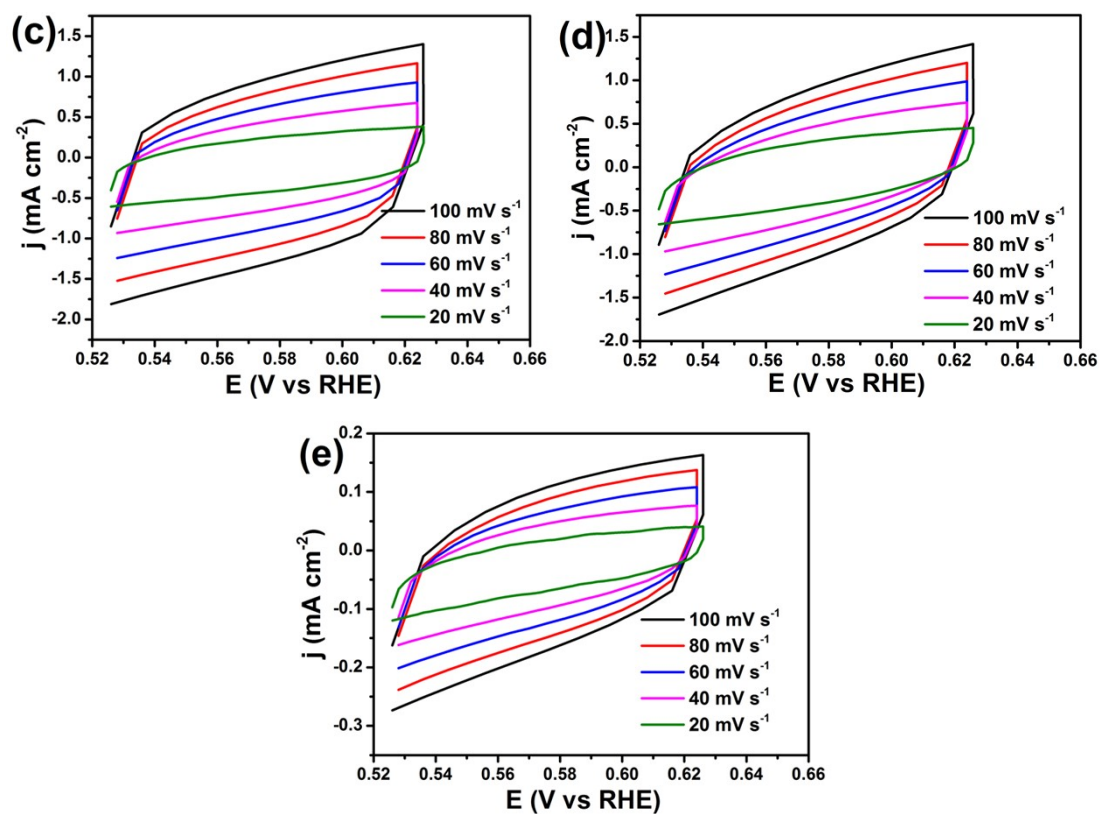

Figure S5. (a,b) SEM images of Ru/NF.

Figure S6. Electrochemical activity specific surface area of different catalysts. Cyclic voltammograms of (a) RuNi-20/NF (b) RuNi-10/NF (c) RuNi-30/NF (d) Ru/NF and (e) Ni/NF with different rates from 20 mV s^{-1} to 100 mV s^{-1}.
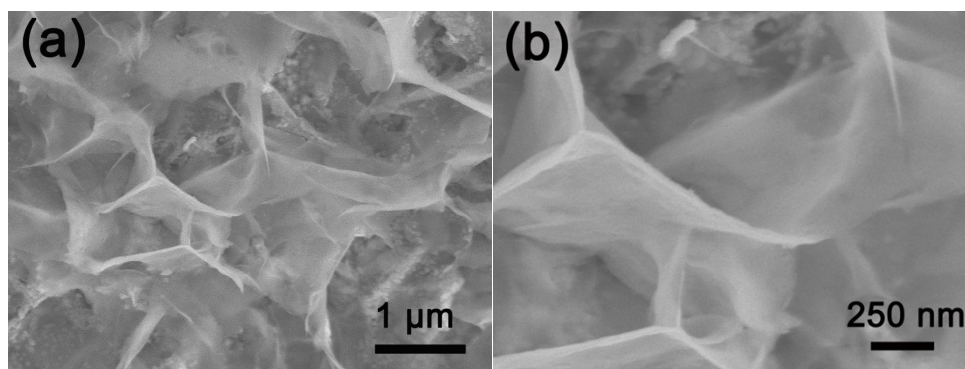
Figure S7. (a,b)The SEM images of the RuNi-20/NF after the stability test.
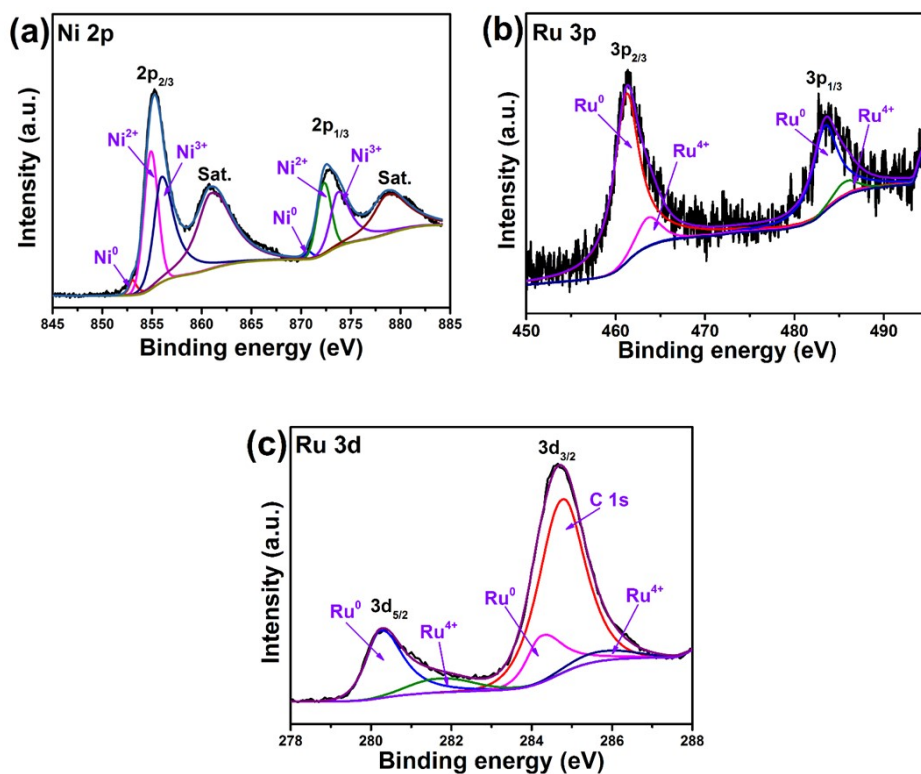
Figure S8. XPS spectrum of (a) Ni 2p, (b) Ru 3p and (c) Ru 3d of of RuNi-20/NF after stability tests.

Table S1. Summary of recently reported HER catalysts in alkaline electrolytes.

Catalyst	Electrolyte	Current density (mA cm^{-2})	η /mV	Ref.
RuNi alloy	**1.0 M KOH**	**-10**	**21**	**This work**
Pt$_3$Ni$_2$-NWs-S/C	1.0 M KOH	-10	42	1
RuP$_2$@NPC	1.0 M KOH	-10	52	2
Co@Ir/NC	1.0 M KOH	-10	121	3

Catalyst				
$Ir_{0.5}W_{0.5}$	0.1 M KOH	-10	29	4
$Ni_{0.93}Ir_{0.07}$/rGO	1.0 M KOH	-10	32.5	5
$Ru/Ni(OH)_2$/NF	1.0 M KOH	-10	25	6
M-Co NPs@Ru SAs/NC	1.0 M KOH	-10	34	7
Ru/MoO_{2-x}	1.0 M KOH	-10	29	8
NiO/Ru@PNS	1.0 M KOH	-10	39	9
Pd@Ru NRs	1.0 M KOH	-10	30	10
Ru/Ru_2P	1.0 M KOH	-10	43.4	11

Table S2. Summary of the activity and stability of the recently reported electrocatalysts at large current density.

Catalyst	Overpotential	Stability	**Ref.**
RuNi alloy	21 mV at 10 mA cm^{-2} 76 mV at 100 mA cm^{-2} 222 mV at 1000 mA cm^{-2} 323 mV at 2000 mA cm^{-2}	150 h	**This work**
$NiCoP/NiCoS_x$	68 mV at 10 mA cm^{-2} 144 mV at 100 mA cm^{-2} 222 mV at 500mA cm^{-2}	110 h	12
$CoP/Ni(OH)_2$	108 mV at 100 mA cm^{-2} 175 mV at 500 mA cm^{-2}	70 h	13
$NiCoS_x$@CoCH NAs/NF	55 mV at 10 mA cm^{-2} 438 mV at 1000 mA cm^{-2}	500 h	14
NiCoV-LTH/NF	213 mV at 10 mA cm^{-2} 327 mV at 100 mA cm^{-2} 442 mV at 500 mA cm^{-2}	20 h	15
$NF@Co_{1-x}V_xP$	46 mV at 10 mA cm^{-2} 226 mV at 400 mA cm^{-2}	24 h	16
A-NiCo LDH/NF	151 mV at 100 mA cm^{-2} 286 mV at 500 mA cm^{-2}	72 h	17

	381 mV at 1000 mA cm^{-2}		
Ni$_{2(1-x)}$Mo$_{2x}$P	68 mV at 10 mA cm^{-2} 144 mV at 100 mA cm^{-2} 222 mV at 500mA cm^{-2}	160 h	18
a-MoWS$_x$/N-RGO	222 mV at 1000 mA cm^{-2}	24 h	19
3F-FeP	191 mV at 100 mA cm^{-2} 261 mV at 500 mA cm^{-2} 302 mV at 1000mA cm^{-2}	24 h	20
Ni NWs/Ni/CM	160 mV at 100 mA cm^{-2} 248 mV at 500 mA cm^{-2} 317 mV at 1000mA cm^{-2}	160 h	21
MoS$_2$–Mo$_2$C/Mo	56 mV at 10 mA cm^{-2} 446 mV at 1000 mA cm^{-2}	20 h	22
Pt@Cu	35 mV at 10 mA cm^{-2} 438 mV at 1000 mA cm^{-2}	10 h	23
Cr-CoP-NR/CC	38 mV at 10 mA cm^{-2} 309 mV at 500 mA cm^{-2}	20 h	24

References

1. P. Wang, X. Zhang, J. Zhang, S. Wan, S. Guo, G. Lu, J. Yao and X. Huang, Precise tuning in platinum-nickel/nickel sulfide interface nanowires for synergistic hydrogen evolution catalysis, *Nat Commun*, 2017, **8**, 14580.

2. Z. Pu, I. S. Amiinu, Z. Kou, W. Li and S. Mu, RuP$_2$-Based Catalysts with Platinum-like Activity and Higher Durability for the Hydrogen Evolution Reaction at All pH Values, *Angew Chem Int Ed*, 2017, **56**, 11559-11564.

3. D. L. Li, Z. Zong, Z. H. Tang, Z. Liu, S. W. Chen, Y. Tian and X.

F. Wang, Total Water Splitting Catalyzed by Co@Ir Core-Shell Nanoparticles Encapsulated in Nitrogen-Doped Porous Carbon Derived from Metal Organic Frameworks, *ACS Sustainable Chemistry & Engineering*, 2018, **6**, 5105-5114.

4. L. Fu, X. Hu, Y. Li, G. Cheng and W. Luo, IrW nanobranches as an advanced electrocatalyst for pH-universal overall water splitting, *Nanoscale*, 2019, **11**, 8898-8905.

5. S. Zhang, X. Zhang, X. R. Shi, F. Zhou, R. H. Wang and X. J. Li, Facile fabrication of ultrafine nickel-iridium alloy nanoparticles/graphene hybrid with enhanced mass activity and stability for overall water splitting, *Journal of Energy Chemistry*, 2020, **49**, 166-173.

6. Q. Q. Chen, X. Yang, C. C. Hou, K. Li and Y. Chen, Inlay of ultrafine Ru nanoparticles into a self-supported $Ni(OH)_2$ nanoarray for hydrogen evolution with low overpotential and enhanced kinetics, *J Mater Chem A*, 2019, **7**, 11062-11068.

7. H. Zhang, H. Su, M. A. Soldatov, Y. Li, X. Zhao, M. Liu, W. Zhou, X. Zhang, X. Sun, Y. Xu, P. Yao, S. Wei and Q. Liu, Dynamic CoRu Bond Shrinkage at Atomically Dispersed Ru Sites for Alkaline Hydrogen Evolution Reaction, *Small*, 2021, **17**, 2105231

8. C. Li, H. Jang, M. G. Kim, L. Q. Hou, X. Liu and J. Cho, Ru-incorporated oxygen-vacancy-enriched MoO_2 electrocatalysts for

hydrogen evolution reaction, *Applied Catalysis B-Environmental*, 2022, **307**, 121204.

9. C. L. Zhong, Q. W. Zhou, S. W. Li, L. Cao, J. C. Li, Z. H. Shen, H. X. Ma, J. G. Liu, M. H. Lu and H. G. Zhang, Enhanced synergistic catalysis by a novel triple-phase interface design of NiO/Ru@Ni for the hydrogen evolution reaction, *J Mater Chem A*, 2019, **7**, 2344-2350.

10. Y. Luo, X. Luo, G. Wu, Z. Li, G. Wang, B. Jiang, Y. Hu, T. Chao, H. Ju, J. Zhu, Z. Zhuang, Y. Wu, X. Hong and Y. Li, Mesoporous Pd@Ru Core-Shell Nanorods for Hydrogen Evolution Reaction in Alkaline Solution, *ACS Appl Mater&Interfaces*, 2018, **10**, 34147-34152.

11. Z. Liu, Z. Li, J. Li, J. Xiong, S. F. Zhou, J. W. Liang, W. W. Cai, C. W. Wang, Z. H. Yang and H. S. Cheng, Engineering of Ru/Ru_2P interfaces superior to Pt active sites for catalysis of the alkaline hydrogen evolution reaction, *J Mater Chem A*, 2019, **7**, 5621-5625.

12. W. Han, F. Zhang, L. Qiu, Y. Qian, S. Hao, P. Li, Y. He and X. Zhang, Interface engineering of hierarchical $NiCoP/NiCoS_x$ heterostructure arrays for efficient alkaline hydrogen evolution at large current density, *Nanoscale*, 2022, **14**, 15498–15506.

13. F.-L. Wang, Y.-N. Zhou, J.-Y. Lv, B. Dong, X.-Y. Zhang, W.-L. Yu, J.-Q. Chi, Z.-X. Wu, L. Wang and Y.-M. Chai, Nickel

hydroxide armour promoted CoP nanowires for alkaline hydrogen evolution at large current density, *Int J Hydrogen Energ*, 2022, **47**, 1016-1025.

14. X. Zhang, R. Zheng, M. Jin, R. Shi, Z. Ai, A. Amini, Q. Lian, C. Cheng and S. Song, $NiCoS_x$@Cobalt Carbonate Hydroxide Obtained by Surface Sulfurization for Efficient and Stable Hydrogen Evolution at Large Current Densities, *ACS Appl Mater& Interfaces*, 2021, **13**, 35647-35656.

15. Q. Liu, J. Huang, D. Yang, Y. Feng, G. Li, X. Zhang, Y. Zhang, G. Xu and L. Feng, Formation of porous NiCoV-LTH nanosheet arrays by in situ etching of nickel foam for the hydrogen evolution reaction at large current density, *Dalton Transactions*, 2021, **50**, 72-75.

16. M. Yang, C. Shang, F. Li, C. Liu, Z. Wang, S. Gu, D. Liu, L. Cao, J. Zhang, Z. Lu and H. Pan, Synergistic electronic and morphological modulation on ternary $Co_{1-x}V_xP$ nanoneedle arrays for hydrogen evolution reaction with large current density, *Science China-Materials*, 2021, **64**, 880-891.

17. H. Yang, Z. Chen, P. Guo, B. Fei and R. Wu, B-doping-induced amorphization of LDH for large-current-density hydrogen evolution reaction, *Applied Catalysis B: Environmental*, 2020, **261**, 118240.

18. L. Yu, I. K. Mishra, Y. Xie, H. Zhou, J. Sun, J. Zhou, Y. Ni, D. Luo, F. Yu, Y. Yu, S. Chen and Z. Ren, Ternary $Ni_{2(1-x)}Mo_{2x}P$ nanowire arrays toward efficient and stable hydrogen evolution electrocatalysis under large-current-density, *Nano Energy*, 2018, **53**, 492-500.

19. D. Zhang, F. Wang, W. Zhao, M. Cui, X. Fan, R. Liang, Q. Ou and S. Zhang, Boosting Hydrogen Evolution Reaction Activity of Amorphous Molybdenum Sulfide Under High Currents Via Preferential Electron Filling Induced by Tungsten Doping, *Advanced Science*, 2022, **9**, 2202445.

20. X.-Y. Zhang, F.-T. Li, J. Zhao, B. Dong, F.-L. Wang, Z.-X. Wu, L. Wang, Y.-M. Chai and C.-G. Liu, Tailoring the d-band centers of FeP nanobelt arrays by fluorine doping for enhanced hydrogen evolution at high current density, *Fuel*, 2022, **316**, 123206.

21. D. Gao, S. Ji, H. Wang, X. Wang, V. Linkov and R. Wang, Copper mesh supported nickel nanowire array as a catalyst for the hydrogen evolution reaction in high current density water electrolysis, *Dalton Transactions*, 2022, **51**, 5309-5314.

22. C. Jian, Q. Cai and W. Liu, A three-dimensional macroporous framework molybdenum disulfide-carbide heterojunction for highly efficient electrocatalytic hydrogen evolution at high current densities, *Chem Commun*, 2021, **57**, 11819-11822.

23. Y. Tan, R. Xie, S. Zhao, X. Lu, L. Liu, F. Zhao, C. Li, H. Jiang, G. Chai, D. J. L. Brett, P. R. Shearing, G. He and I. P. Parkin, Facile Fabrication of Robust Hydrogen Evolution Electrodes under High Current Densities via Pt@Cu Interactions, *Adv Funct Mater*, 2021, **31**, 2105579.

24. L. Zhang, J. Zhang, J. Fang, X.-Y. Wang, L. Yin, W. Zhu and Z. Zhuang, Cr-Doped CoP Nanorod Arrays as High-Performance Hydrogen Evolution Reaction Catalysts at High Current Density, *Small*, 2021, **17**, 2100832.